scientific reports

Check for updates

OPEN

Effects of temperature and confinement mechanisms on the deformation of selective laser melting 3D printed SS316 using finite element analysis

Ambuj Saxena[1], Neeraj Mishra[2], Shashi Prakash Dwivedi[3], Shubham Sharma[4,5,6]✉, N. Beemkumar[7], Ankit Kedia[8], V. Nagabhushana Rao[9], Parveen Kumar[10], Abhinav Kumar[11], Ehab El Sayed Massoud[12] & Jasmina Lozanovic[13]✉

The confined constrained deformation behavior of SLM 3D printed SS316 has been analyzed at room temperature, 200 °C, 400 °C, 600 °C, and 800 °C temperature through static ball indentation finite element analysis technique model (load range 5 kN to 50 kN). The constrained confined deformation behavior analysis of SLM 3D printed SS316L steel specimen through static indentation process helps understand their mechanical response under localized compressive loading. This study helps to understand material plastic flow behavior at the time of low-velocity foreign object strike. Further, the results were analysed in terms of Meyer's hardness (H_M), constraint factor (CF), lip height, average strain, strain hardening index (p), and indentation strength coefficient (A). The finite element analysis (FEA) results are validated with the analytical models (Johnson's Expansion cavity model (ECM) and Richmond's fully-plastic model (FPM)) and experimental results. The results revealed that the Meyer's hardness was reduced 10.20%, 21.68%, 42.07% and 66.62% at 200 °C, 400 °C, 600 °C, and 800 °C respectively, compared with room temperature. Further, the lip height was increased by 24.34%, 51.40%, 98.29% and 129.22% at 200 °C, 400 °C, 600 °C, and 800 °C respectively, compared with room temperature. The constraint factor (CF) was 2.539, 2.625, 2.711, 2.961 and 3.211 at room temperature, 200 °C, 400 °C, 600 °C, and 800 °C temperature respectively under confined constrained deformation condition. Further, the CF was increased with increase in the temperature. The yield strength of the investigated material was decreased by 8.60%, 27.08%, 55.44% and 75.45% at the 200 °C, 400 °C, 600 °C, and 800 °C respectively. Further, the compressive strength was decreased by 9.94%, 30.01%, 61.72% and 88.41% at the 200 °C, 400 °C, 600 °C and 800 °C respectively. The FEA model results show the good agreement with the experimental results with less than 5% percentage difference. This shows the good prediction capability of the developed FEA model. The constrained confined deformation behavior study on SLM 3D printed SS316L study is the prime focus of the current investigation which confirms the suitability of material under foreign objects impact conditions like aerospace and defence sector.

Keywords Confined constrained deformation, Static indentation process, Constraint factor, Lip height, Expansion cavity model, Fully-plastic model

[1]Department of Mechanical Engineering, G. L. Bajaj Institute of Technology and Management, Greater Noida 201306, India. [2]Center for Artificial Intelligence and Robotics, Madhav Institute of Technology & Science, Gwalior 474005, India. [3]Department of Mechanical Engineering, Lloyd Institute of Engineering and Technology, Greater Noida, India. [4]Department of Technical Sciences, Western Caspian University, Baku, Azerbaijan. [5]Centre for Research Impact and Outcome, Chitkara University Institute of Engineering and Technology, Chitkara University, Rajpura 140401, Punjab, India. [6]Jadara University Research Center, Jadara University, Irbid, Jordan. [7]Department of Mechanical Engineering, School of Engineering and Technology, JAIN (Deemed to be University), Bangalore, Karnataka, India. [8]Department of Mechanical & Aerospace Engineering, NIMS Institute of Engineering & Technology, NIMS University Rajasthan, Jaipur, India. [9]Department of Mechanical Engineering, Raghu Engineering College, Vishakhapatnam 531162, Andhra Pradesh, India. [10]Department of Mechanical Engineering, Chandigarh

College of Engineering, Chandigarh Group of Colleges, Jhanjeri, Mohali 140307, Punjab, India. [11]Department of Nuclear and Renewable Energy, Ural Federal University Named After the First President of Russia, Boris Yeltsin, 19 Mira Street, Ekaterinburg 620002, Russia. [12]College of Applied Sciences, King Khalid University, Dhahran Al-Janoub, Kingdom of Saudi Arabia. [13]Department of Engineering, FH Campus Wien - University of Applied Sciences, Vienna 1100, Austria. ✉email: shubhamsharmacsirclri@gmail.com; shubham543sharma@gmail.com; jasmina.lozanovic@fh-campuswien.ac.at

At present time, complex industrial and defence metal components are fabricated with the help of selective laser melting (SLM), an advanced additive manufacturing technique[1,2]. The fused metal powder rapid cooling rate (10^3–10^8K/s) of SLM process results in a refined microstructure of printed objects[3–5]. In defence applications body armor, protective gear, and anti-Drone Systems are fabricated with the help of SLM 3D printing[1]. Further, the SS316L powder has been utilized for applications as mentioned earlier. Ergene et al.[6] investigated the mechanical performance of Ti6Al4V cellular structures, including different unit cell forms such as honeycomb, re-entrant, hybrid (honeycomb + re-entrant), and chiral structures manufactured with selective laser melting. Further the results revealed that the highest values for compressive strength, energy absorption, and specific energy absorption were observed in re-entrant structures, while hybrid structures had the highest elasticity modulus values. Ergene[7] uses IN 718 and Ti-6Al-4V to SLM 3D print cellular structures used as scaffold and implant core structure in the biomedical field were designed with different infill rates (100%, 73.4% and 42.6%). Further, the results revealed that the material type, relative density and building height of the parts are the most significant factors that affect the residual stress and displacement values which occur on the parts during SLM 3D printing. The SLM 3D print material exhibited modified mechanical, physical and chemical properties which can provide unique engineering solutions[8]. Moreover, earlier mentioned applications are subjected to high strain rate (10^2 to 10^4 s^{-1}) phenomena like foreign object damage, ballistic penetration, high speed sliding wear, and ballistic penetration[9–11]. In the actual war zone scenario, the plastic deformation of material under high strain rate is constrained due to confined deformation[11]. Further, this confined constrained deformation behavior of a material cannot be predicted with the help of uniaxial deformation testing like, compression, tensile and Split-Hopkinson pressure bar testing[9,11]. The static and dynamic indentation techniques have been utilized to understand the constrained confined deformation behavior of materials[10]. Hence, the available uniaxial testing cannot predict the confined constrained deformation behavior. The required pressure for the uniaxial compression plastic deformation is much less than the pressure required for the constrained confined plastic deformation due to the resistance of the surrounding material layer[12–14]. Further, the constraint factor (CF) is the factor by which the resistance to plastic deformation under confined constrained conditions is higher than the resistance to plastic deformation under uniaxial conditions[14–16]. Moreover, the true stress in the constrained confined deformation process are the 2 to 3 times the flow stresses developed under uniaxial deformation process[16,17]. Several studies focus on the determination of constraint factors for armor-grade steel, titanium alloys, Inconel alloys, composite materials and other materials[18–20]. Further, the result revealed that CF varied from 2.6 to 3.1 for ductile materials[18–20]. Moreover, the CF is over 3.0 for metallic glass[16]. The existing literature are showing the effect of average strain on Meyer's hardness and CF at the room temperature only to understand the confined constrained conditions deformation behavior. Kumaraswamy et al.[21,22] and Saxena et al.[9] revealed the temperature dependency of constraint factor for IN718 and Armox 500T respectively. The static indentation test was also helpful in the prediction of plastic flow behavior of materials. Rom et al.[23] uses a data driven approach that leverages machine learning and static indentation based finite element analysis was used to construct a model called 'Brilearn' to predicts the stress–plastic strain curve of metallic materials. Saxena et al.[24] developed the representative volume element (RVE) based finite element analysis (FEA) model and macro-mechanical static indentation FEA model to analyze the plastic deformation of developed composite material under constrained confined deformation conditions at a load range of 4.90–49.03 kN. The above mentioned literature[23,24] revealed that the confined constrained plastic deformation behavior can predicted with the help of static indentation process. Further, the static indentation FEA prediction can save the time of experimentation. The data related to elevated temperature effect on the confined constrained conditions deformation behavior are rarely available in the literature for materials and 3D printed objects. The dynamic plastic flow behavior with adiabatic deformation conditions also can be evaluated through constraint factor (CF) which is evaluated through static indentation process[8].

In the current investigation, temperature dependent (room temperature, 200 °C, 400 °C, 600 °C and 800 °C) constrained confined plastic deformation of SLM 3D printed SS316L steel has been investigated through static indentation process simulation with Abaqus finite element code. Further, the behavior of constraint factor (CF) and Meyer's hardness (H_M) against average strain has also been investigated for different temperatures (room temperature, 200 °C, 400 °C, 600 °C and 800 °C). The static indentation finite element analysis (FEA) results also validated with experimental static indentation process. Moreover, the lip height behavior has also been investigated against average strain at different temperature ranges (room temperature (25 °C), 200 °C, 400 °C, 600 °C and 800 °C). As we discussed earlier, the deformation under foreign object damage and ballistic penetration conditions is subjected to confined constrained deformation behavior. The reviewed literature also indicates that studies on the confined constrained deformation behavior of 3D-printed objects are currently unavailable. Hence this study fulfils this gap and confirms the suitability of SLM 3D printed material under foreign object impact conditions like the aerospace and defence sector.

Experimental details

Under investigation material powder for 3D printing

In the present investigation, SS316L steel powder has been utilized to print the compression test and static indentation test specimen. Further, the main advantage of SS316L steel powder is the biocompatibility with

Elements	Cr	Ni	Mo	C	N	Fe
Weight percentage (%)	17.6	15.2	2.15	0.032	0.15	Balance

Table 1. Chemical composition of SS316L.

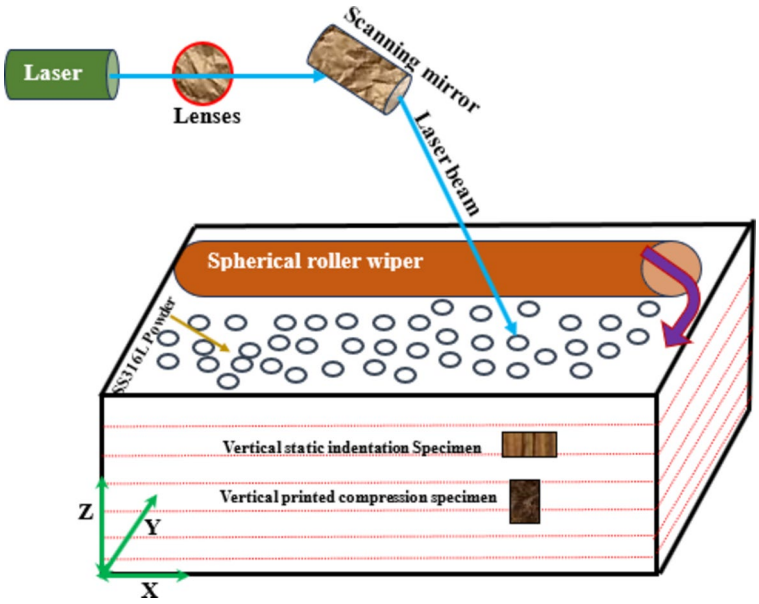

Fig. 1. Schematic diagram of selective laser melting (SLM) 3D printing.

Process Parameters	Value
Laser power (W)	220
Scanning speed (m/s)	1.5
Hatch spacing (μm)	120
Laser spot size (μm)	75
Layer thickness (μm)	50
Pre-heating temperature (°C)	100
Part bed temperature (°C)	250

Table 2. Process parameters used in 3D printing.

human tissues without harmful effects. The as received SS316L steel powder size range was between 35 and 70 μm. Table 1 exhibited the different compositions weight percentages in as received SS316L steel powder.

Printing technique

Selective lase melting (SLM) technique has been utilized to three-dimensional printing of the static indentation and compression test specimens. Figure 1 shows the schematic diagram of the selective laser melting 3 D printing technique. In this technique, fine SS316L steel powder particles were melted with the help of high power laser beam to build the layer by layer object. The required object was modelled with the help of computer aided design software and saved in the stereolithography (.stl) file format. Further, the 3-dimensional printer accept only .stl file format for 3D printing of required object. The. stl format was sliced the required object geometry in to a number of layers and converted the desired information in to machine instructions. Moreover, the thin layered SS316L steel powder particles was melted and fused by a high-power laser beam on the build platform. Further, the laser also traces the cross-sectional geometry to form the entire part. In the present investigation, DMP Flex 2000 3D printer (Manufacturer: 3D systems) with $140 \times 140 \times 115$ mm build volume has been utilized to 3D print the SS316L static indentation and compression test specimens in the vertical direction (shown in Fig. 1).

The process parameters for SLM 3D printing of static indentation and compression test specimens are mentioned in Table 2.

Low strain rate testing at $10^{-3}s^{-1}$ strain rate

In the present investigation, two types of low strain rate testing were performed on SLM 3D printed SS316L specimens at 10^{-3} s^{-1}. Firstly, the compression testing was performed on the SLM 3D printed SS316L specimens at room temperature (25 °C), 200 °C, 400 °C, 600 °C and 800 °C by utilizing the Walter + Bai Ag universal testing machine (UTM). The UTM was consisted a tubular furnace up to 1200 °C capacity for performing the compression test at elevated temperatures. The sample size for compression testing was taken as 5 mm diameter and 10 mm length (length/diameter ratio is taken as 2). The SLM 3D printed SS316L steel specimens were compressed up to 70 to 75%. Further, the friction at specimen-platen interface was reduced by adding 0.1 mm layer of molybdenum disulfide (MoS_2) powder particles. The flow stress vs. true plastic strain was evaluated from load-compression data as per Saxena et al.[25] investigations.

In the present study static indentation experiment test was carried out at the 50 kN load on a standard 'FIE' Computerized Fully Automatic Brinell Hardness Tester, Model B3000-PC-FA using a non-deformable Tungsten carbide spherical ball of 10 mm diameter at room temperature for SLM 3D printed SS316L steel. Further, the sample size for the static indentation test was 25 × 25 × 25 mm. Top and Bottom surfaces of the test sample have been carefully ground and polished to ensure flatness and parallelism within 1 µm. The strain rate for performing the static indentation test was taken as 10^{-3} s^{-1}. The hardness of the indentation ball was taken as 2020 HV which is five times greater than under investigated material. The applied indentation load on the under-investigated material was estimated with a ± 1 N accuracy-enabled load cell. The experimental set-up of the static indentation test (Brinell hardness tester) is shown in Fig. 2(a). The maximum load capacity of the machine was extended up to 50kN. The dwell time (the time that the applied test load is maintained on the specimen during the test) was 10 s. The dimensions (diameter, depth and lip height etc.) of the residual impressions formed during the static indentation test were measured perusing crater profile by using a Mitutoyo profile measuring machine to an accuracy of ± 1 µm. Further, the crater profiles help to measure the diameter, crater depth and lip height at applied load as shown in Fig. 2(b). The estimated crater depth is further used to evaluate Meyer's hardness H_M and average strain ε_{av}experienced by the specimen during the indentation[9–11,21,22]. The Meyer's hardness (H_M) and average strain (ϵ_{avg}) was estimated with the help of Eqs. (1) and (2) respectively[9–11,21,22].

$$H_M = \frac{P}{\frac{\pi}{4}(W)^2} \quad (1) \qquad (1)$$

Where, P = applied indentation load, W = crater diameter.

$$\epsilon_{avg} = 0.2\frac{W}{D} \quad (2) \qquad (2)$$

where, D = spherical indenter diameter.

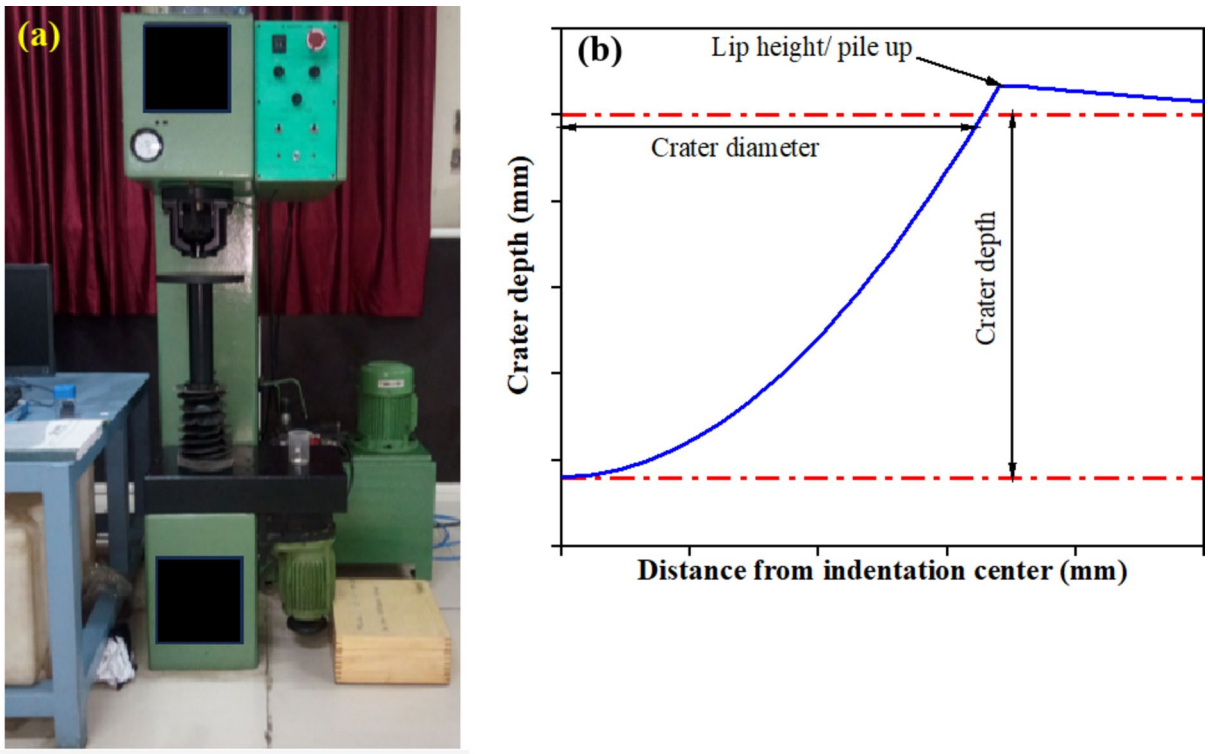

Fig. 2. (**a**) Static indentation experimental test setup, (**b**) Schematic diagram of static indentation crater profile.

Temperature	Indentation test (FEA)				Experimental compression test				
	Strain range (%)	*p*	A (MPa)	Lip height (μm)	Strain range (%)	0.2% yield strength (MPa)	*n*	K (MPa)	Compressive strength (MPa)
Room Temperature	3.61–10.32	0.20	1474.57	25.46	0.2–11.56	560.49 ± 11.20	0.134 ± 0.0034	1252.43 ± 25.04	948.37 ± 19.91
200°C	3.78–10.91	0.19	1378.32	32.53	0.2–11.90	514.26 ± 10.28	0.127 ± 0.0032	1125.30 ± 22.51	858.55 ± 18.02
400°C	3.96–11.50	0.18	1288.85	43.08	0.2–12.20	426.79 ± 8.52	0.120 ± 0.0029	900.25 ± 18.01	700.84 ± 14.72
600°C	4.58–13.05	0.16	997.06	74.70	0.2–13.40	317.19 ± 6.34	0.11 ± 0.0028	625.31 ± 12.52	501.03 ± 10.53
800°C	5.20–14.60	0.15	720.00	118.44	0.2–14.60	253.43 ± 5.06	0.085 ± 0.00021	430.02 ± 8.61	366.90 ± 7.71

Table 3. Evaluated material properties for SLM 3D printed SS316 steel at different temperatures.

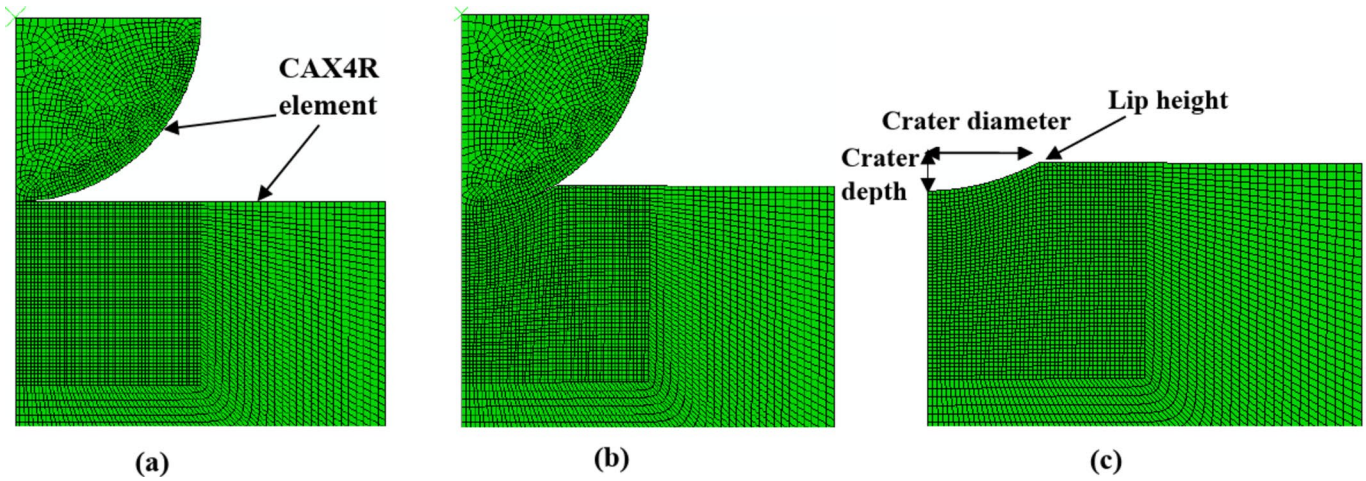

Fig. 3. Meshing of static indentation process model (**a**) before loading, (**b**) after loading, (**c**) crater profile.

The static indentation test has been carried out for the validation of FEA model.

Low strain rate static indentation process finite element analysis

Low strain rate finite element analysis model of static indentation process has been developed by utilizing the Abaqus FEA code. The assembly consist of two main parts rigid non-deformable spherical ball indenter (made with tungsten carbide (WC)) and deformable SLM 3 D printed SS316L steel specimen. The spherical ball indenter was modelled with the 10 mm diameter. Further, the specimen was modelled with the dimension 25 × 25 mm. The indentation load (load range 5–50 kN) was applied on the rigid indenter at the vertical direction. A simulation was run on the room temperature, 200 °C, 400 °C, 600 °C and 800 °C conditions. The material properties utilised in the development of finite element analysis model was taken from the experimental compression testing results which were mentioned in Table 3. The Hollomon power law parameters (strength coefficient (K) and strain hardening exponent (n)) were evaluated from experimental compressive flow stress vs. true plastic strain curve at room temperature, 200 °C, 400 °C, 600 °C and 800 °C temperature and mentioned in Table 3 (later explained in Sect. "Influence of temperature on uniaxial plastic deformation process"). The Hollomon power law parameters are useful in predicting the deformation behavior of the under-investigated material. The evaluated Hollomon power law parameters provide to finite element analysis code as input material properties to predict the static indentation behavior at room temperature, 200 °C, 400 °C, 600 °C and 800 °C. Figure 3(a), (b) and (c) show the meshed FEA model assembly of the static indentation process at unloading conditions, loading conditions, and developed crater profile conditions respectively. Further, a four-node axisymmetric bi-linear element CAX4R was utilized in the meshing of spherical indenter and deformable specimens[17,19]. The CAX4R element reduces the computational time and converses the data faster. Figure 3(a-c) revealed that mesh density was high at the indenter specimen interface. Further, the mesh density was coarse at the transition area remote from the interaction area. The stress-strain was not critical at the remote areas.

The spherical indenter and deformable specimen consist 1275 and 5752 nodes respectively. Further, the spherical indenter and deformable specimen consist 1228 and 5613 elements respectively. The $U_X = 0$, $U_Y \neq 0$, $R_Z = 0$ boundary condition was given to the axisymmetric axis of the specimen and reference point of the rigid indenter. Further, $U_X \neq 0$, $U_Y = 0$, $R_Z = 0$ boundary condition was given to the base of the specimen as shown in Fig. 4. Here, U_X, U_Y are displacement along the X and Y direction and R_Z is rotation about the Z direction. The indentation load was given on the reference point of the indenter as shown in Fig. 4. The indentation load was incrementally applied on the specimen for the step time 1. A general static solver was utilized to run the simulation. Further, a master and slave contact interaction were provided at the indenter/specimen interface. The hard interaction property was defined between indenter and specimen. The indenter and specimen surface were

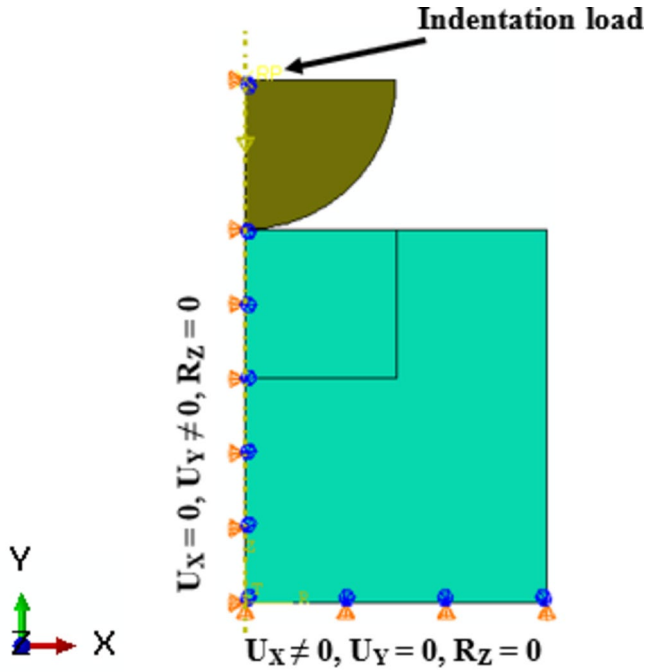

Fig. 4. Loading and boundary conditions for static indentation process FEA model.

taken as master and slave surface respectively. The crater depth, crater diameter and lip height were measured with the help of Figs. 2(b) and 3(c).

Results and discussion

Influence of temperature on SLM 3D printed SS316L steel confined constrained behavior

The SLM 3D printed SS316L steel, Meyer's hardness (H_M) vs. average strain (ϵ_{avg}) was evaluated with the help of Eqs. (1) and (2) respectively for the load range 5 to 50 kN at room temperature, 200 °C, 400 °C, 600 °C and 800 °C. The Meyer's hardness (H_M) and average strain (ϵ_{avg}) were evaluated with the help of SLM 3D printed SS316L steel crater diameter for the load range 5 to 50 kN at room temperature, 200 °C, 400 °C, 600 °C and 800 °C.

Figure 5(a), (b), (c), (d) and (e) shows the SLM 3D printed SS316L steel crater profile graph and deformed shaped (at 50 kN load) generated through static indentation process FEA model at room temperature, 200 °C, 400 °C, 600 °C and 800 °C respectively for load range 5 to 50 kN. Further, the figures revealed that the indented crater depth and diameter were increased with an increase the indentation load and temperature. The maximum crater depth was achieved at the 800 °C rather than room temperature, 200 °C, 400 °C, and 600 °C for the complete load range 5 to 50 kN. The SLM 3D printed material loses the material properties with the increase in the temperature. Figure 6 shows the Meyer's hardness vs. Average strain graph (generated by FEA static indentation process model) for SLM 3D printed SS316L steel at different temperatures (room temperature, 200 °C, 400 °C, 600 °C and 800 °C). The average strain (estimated during the static indentation process) was taken equivalent to the true plastic strain which is experienced by the specimen during the uniaxial compression test. The Meyer's hardness was significantly affected by the applied load and temperature. Figure 6 revealed that the Meyer's hardness was increased with the increase in applied indentation load. At a particular temperature, lowest and highest hardness point was estimated at the 5 kN and 50 kN load. The deformation is constrained by the surrounding material. Hence, highest load offers highest surrounding resistance which increased the Meyer's hardness. The estimated trend was in good agreement with Saxena et al.[9,17] and Kumaraswamy et al.[21,22] study.

Meyer's hardness was decreased with the increased in the temperature. Further, the highest Meyer's hardness range was estimated at room temperature and the lower Meyer's hardness was estimated at 800 °C. The maximum estimated Meyer's hardness values for room temperature, 200 °C, 400 °C, 600 °C and 800 °C were 2342.48, 2115.01, 1884.17, 1528.19 and 1171.80 MPa respectively at 50 kN load.

Further the Meyer's hardness was reduced 10.20%, 21.68%, 42.07% and 66.62% at 200 °C, 400 °C, 600 °C and 800 °C respectively. Meyer's hardness was also increased with the increase in average strain. The Meyer's hardness curve was fitted with Hollomon relation ($H_M = A \epsilon_{avg}^{p}$), to evaluate the strain hardening index (p) and indentation strength coefficient (A). The p and A values are mentioned in Table 3 for SLM 3D printed SS316L steel at different temperatures.

The p ana A values are decreased with the increase in the temperature of static indentation process for SLM 3D printed SS316L steel. Further, under investigated material compressed more at elevated temperature which are showing the increased in average strain values. The lip height around the crater impression was shown in Figs. 2(b), 3(c) and 5(a-e). The elevated temperature significantly affected the lip height around the crater impression.

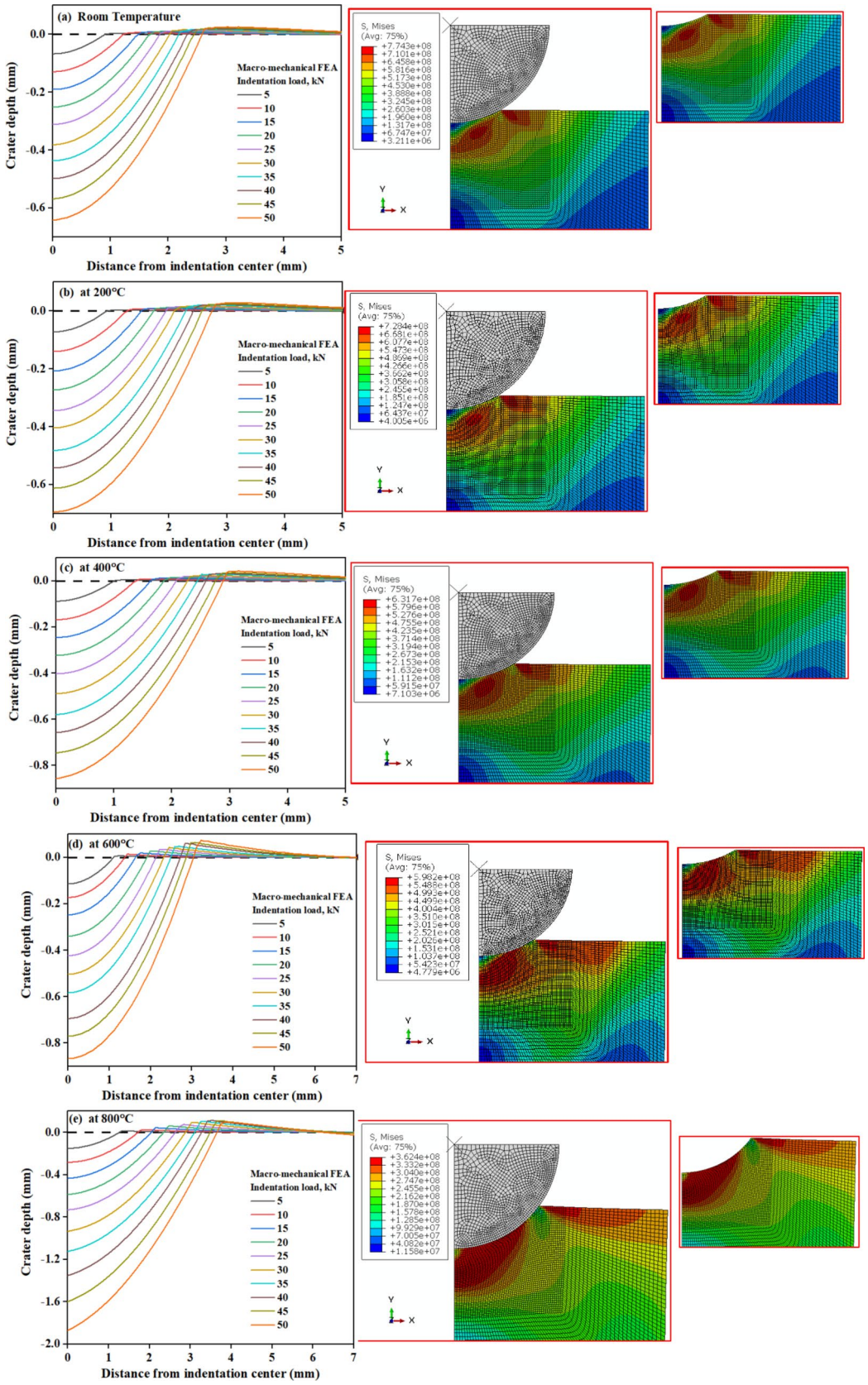

Fig. 5. SLM 3D printed SS316L steel crater profile graph and deformed shaped (at 50 kN load) generated through static indentation process FEA model at (**a**) Room temperature, (**b**) 200 °C, (**c**) 400 °C, (**d**) 600 °C, (**e**) 800 °C.

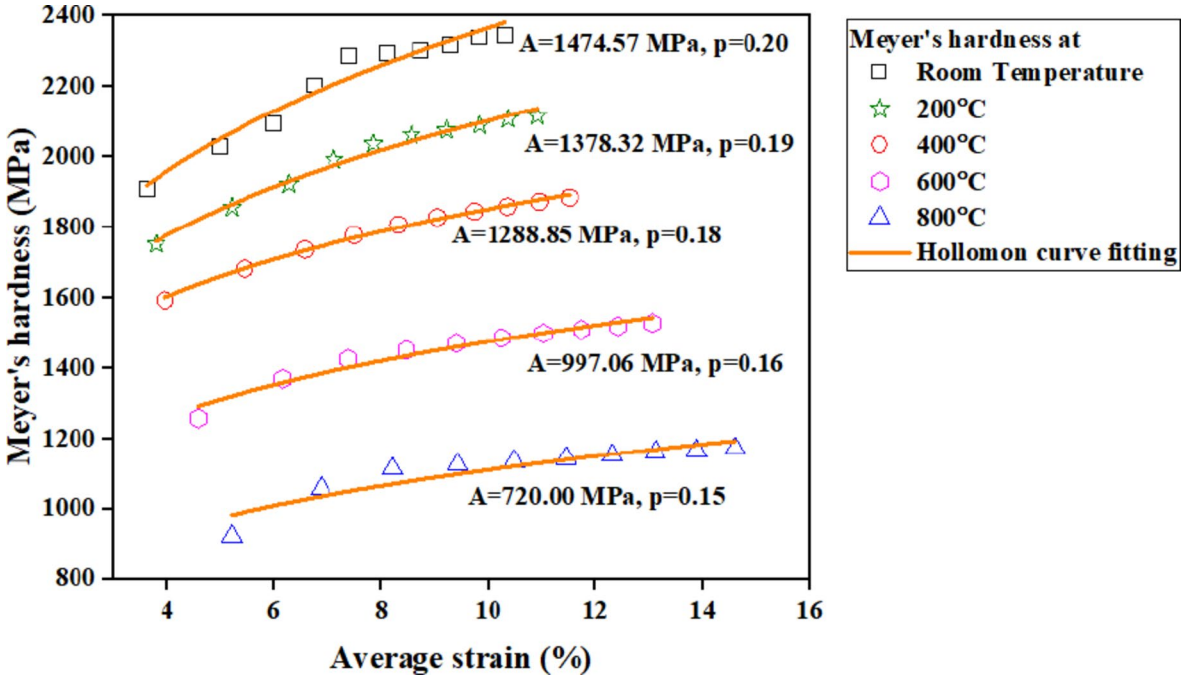

Fig. 6. Meyer's hardness vs. Average strain for SLM 3D printed SS316L steel at different temperatures.

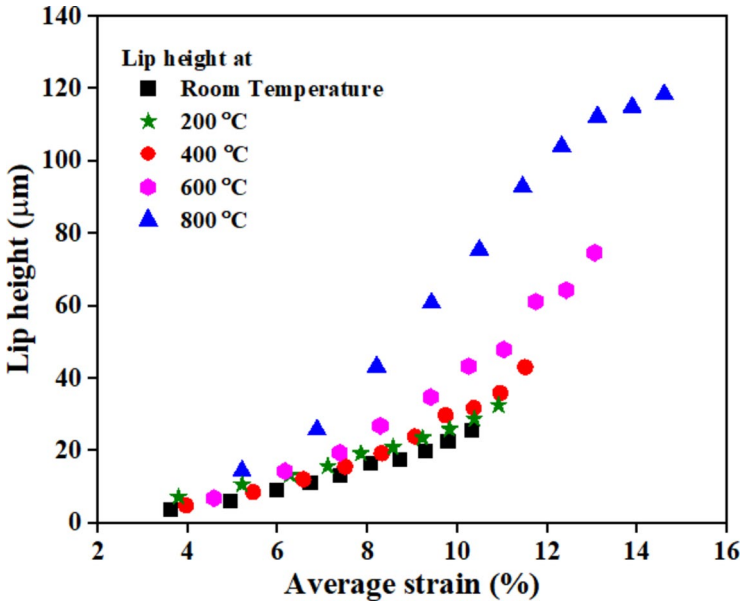

Fig. 7. Lip height vs. average strain for SLM 3D printed SS316L steel at different temperatures.

The lip height was increased with the increase in temperature and average strain as shown in Fig. 7. Figure 7 revealed that the maximum lip height was estimated at 800 °C temperature, 50 kN load and 14.60% average strain. Further, the lip height was increased by 24.34%, 51.40%, 98.29% and 129.22% at 200 °C, 400 °C, 600 °C and 800 °C respectively, compared with room temperature lip height.

Further the lip height was significantly influenced by the static indentation strain hardening exponent (p) and strain hardening exponent (n). The lip height was increased with the decrease in p and n values as mentioned in Table 3. Further, the increased value of p and n was result in decrease of lip height. This is due to the fact that, materials with high strain hardening capability will accommodate more volume of the material displaced by indenter during static indentation, thereby reducing the upward flow around the indentation. The estimated trend was in good agreement with Saxena et al.[9,17] and Kumaraswamy et al.[21,22] study.

Influence of temperature on uniaxial plastic deformation process

In the present investigation, a compression test was performed on the SLM 3D printed SS316L steel specimens at room temperature, 200 °C, 400 °C, 600 °C and 800 °C. The significant influence of temperature was observed on the SLM 3D printed SS316L steel uniaxial plastic deformation as shown in Fig. 8; Table 3. The results revealed that the yield strength of the investigated material was decreased by 8.60%, 27.08%, 55.44% and 75.45% at the 200 °C, 400 °C, 600 °C and 800 °C respectively. Further, the compressive strength was decreased by 9.94%, 30.01%, 61.72% and 88.41% at the 200 °C, 400 °C, 600 °C and 800 °C respectively. The flow stress curves were fitted with the Holloman constitutive equation ($\sigma_f = K\epsilon_{plastic}^{n}$) (where σ_f = flow stress, $\varepsilon_{plastic}$ = true plastic strain, n= strain hardening exponent and K = strength coefficient,) and best-fit values of 'n' and 'K' is listed in Table 3. The yield strength, compressive strength and strength coefficient (K) of the SLM 3D printed SS316L steel was decreased with the increase in the temperature. Further, the average strain and strain hardening exponent was increased with an increase in the temperature. The thermal activation of material has been increased at 800 °C which increases the thermal activation energy which enhances the dislocation mobility in the strain range of 6% and 10% strain. Further, the solute atoms chromium and molybdenum diffuse and interact with moving dislocation at this strain range. Further, this interaction prevents the dislocation movement and leading to an increase in work hardening which is a characteristic of dynamic strain aging. The delayed dynamic recrystallization initiation is delayed which shows that softening effects have not yet significantly reduced the material's strength and contributing to a steeper flow stress slope. The combined effect of dynamic recrystallization and delayed dynamic recrystallization initiation results in, an increase in slope within the mentioned strain range.

Influence of temperature on the constraint factor

The factor by which the resistance to plastic flow underneath the indenter (confined constrained deformation process) is greater than uniaxial flow stress is considered a constraint factor (CF).

At a particular strain, the ratio of Meyer's hardness (at confined constrained deformation conditions) and flow stress (at uniform deformation conditions) estimates the constraint factor (CF). The above-mentioned process of CF evaluation is mentioned in Fig. 9(a), (b) and (c) at room temperature, 400 °C and 800 °C respectively for SLM 3D printed SS316L steel. Further, Fig. 9(d) shows the effect of temperature on the CF at room temperature, 200 °C, 400 °C, 600 °C and 800 °C. The results revealed that the constraint factor was increased with average strain upto the transition strain after that the CF was constant (independent) for the rest of the average strain. This behaviour was observed for SLM 3D printed SS316L steel at room temperature, 200 °C, 400 °C, 600 °C and 800 °C. The transition strain was 8.08, 8.26, 8.34, 8.41 and 9.07% average strain for room temperature, 200 °C, 400 °C, 600 °C and 800 °C respectively. Further, the transition average strain was increased with the increase in the temperature.

The transition strain separated the elastic-plastic zone and fully plastic zone. Further, the CF was dependent on the average strain in the elastic-plastic zone and CF was independent of average strain in the fully-plastic zone.

Moreover, the constraint factor was increased with the increase in the temperature. The CF values at room temperature, 200 °C, 400 °C, 600 °C and 800 °C were 2.539, 2.625, 2.711, 2.961 and 3.211 respectively for SLM 3D printed SS316L steel.

Tirupataiah and Sundararajan[20,23,24] revealed that the CF for different ductile materials varied between 2.6 and 3.0 at room temperature. The present investigation is based on the flow stress vs. true plastic strain curve of 3D printed SS316L at different temperatures. The main reason behind the lower constraint factor (2.565)

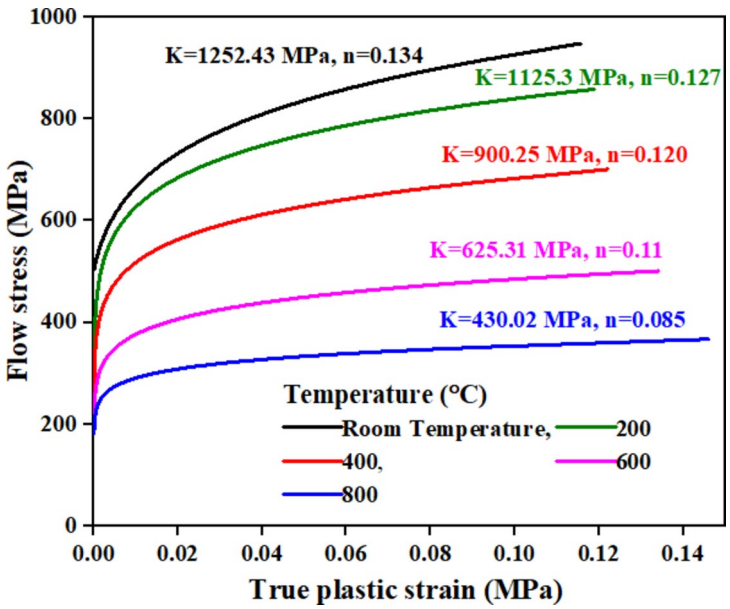

Fig. 8. Flow stress vs. True plastic strain for SLM 3D printed SS316L steel at different temperatures.

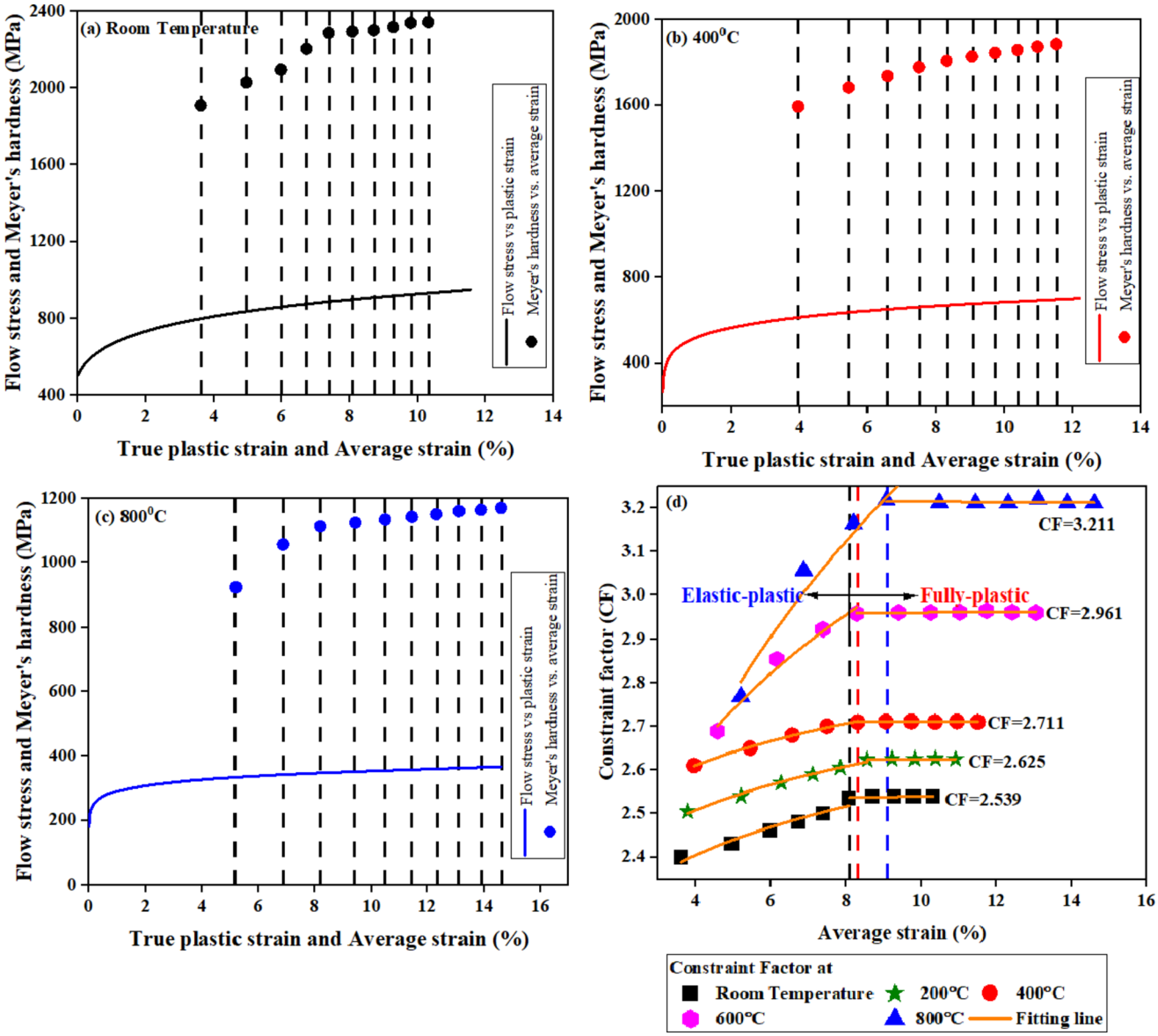

Fig. 9. Estimation of Constraint factor at (**a**) Room temperature, (**b**) 400 °C and (**c**) 800 °C (**d**) Constraint factor variation with average strain for different temperatures.

in 3D-printed SS316L compared to ordinary steel is its microstructure and mechanical properties (which are evaluated through flow stress vs. true plastic strain curve). A fine-grained microstructure with high dislocation density was developed during the SLM process which influences the plastic deformation and stress distribution. Moreover, significant residual stresses from rapid melting and solidification impact the material's yielding and deformation behavior. The presence of porosity and lack of fusion defects further reduces the effective stress intensity at the localized yield portion which lowers the constraint factor.

Validation of static indentation FEA results with analytical models (expansion cavity model (ECM) and fully-plastic model (FPM)) and experimental results

Figure 10(a) shows the schematic diagram of Johnson's expanding cavity model[26]. The specimen/spherical indenter contacting surface radius shows with 'a'. The contacting surface is surrounded by a deformable plastic zone with a radius 'r'. Further, 'da' and 'dr' represent the 'expanded contacting surface radius' and 'deformable plastic zone radius' under the application of indentation load. The atoms of the material surface were moved in a radial direction after the downward movement of the indenter, resulting in the enhancement of the plastic zone size. The relation between indentation mean pressure (H), flow stress (σ_f) and normalized strain (B) can be expressed with the following equation:

$$H = \frac{2}{3}\sigma_f + \frac{2}{3}\sigma_f\left(1 + ln\frac{B}{3}\right) \tag{3}$$

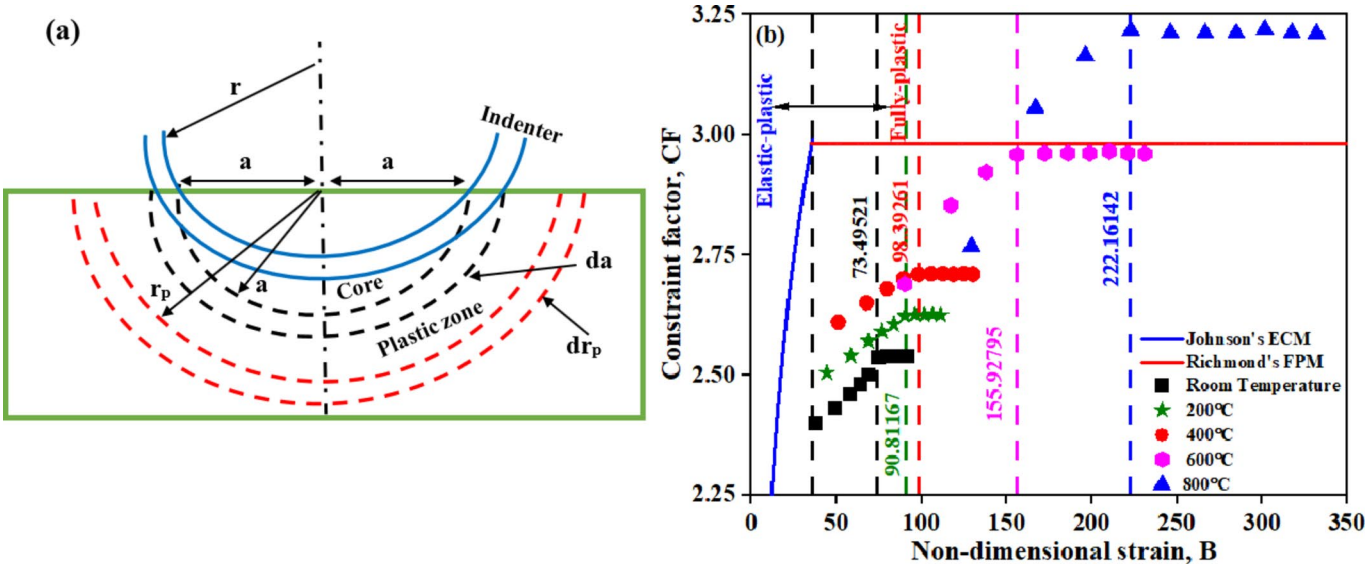

Fig. 10. (**a**) Schematic diagram of the elastic-plastic expanding cavity model, (**b**) Constraint factor vs. non-dimensional strain.

Where,

$$B = \frac{E_e}{\sigma_f}\left(\frac{a}{r}\right) \tag{4}$$

Where, r = radius of the spherical indenter, a = radius of indentation, and E_e = effective modulus Further,

$$\frac{1}{E_e} = \frac{1-\nu^2}{E} + \frac{1-\nu^2}{E_1} \tag{5}$$

Where ν and E are the Poisson's ratio and Young's modulus of SLM 3D printed SS316L steel respectively. Further, the Poisson's ratio and Young's modulus of the tungsten carbide (WC) spherical indenter are 0.23 and 530 GPa respectively[18–20].

The constraint factor (CF) vs. non-dimensional strain (B) graph is shown in Fig. 10(b). Further Johnson's ECM and Richmond's FPM model[27] lines are marked on the CF vs. non-dimensional strain with blue and red lines respectively. The blue line represents the elastic-plastic region and the red line represents the fully-plastic region. The CF was increased with B (elastic-plastic region) up to a transitional non-dimensional strain after that the CF was independent of B (fully-plastic region) for all the temperatures. Figure 10(b) revealed that the transition non-dimensional strain values for room temperature, 200 °C, 400 °C, 600 °C and 800 °C were 73.49, 90.81, 98.39, 155.92 and 222.16 respectively. The SLM 3D printed SS316L steel followed ECM and FPM model trends at all the investigated temperatures. The plastic zone occurs early at room temperature than 200 °C, 400 °C, 600 °C and 800 °C respectively under confined constrained deformation behavior. Further, the plastic zone delays at elevated temperatures.

The developed SLM 3D printed SS316L steel static indentation process FEA results were also validated with experimental results as shown in Fig. 11. The static indentation experiments were conducted on a 50kN load at room temperature.

Figure 11 shows the indentation crater profile generated by experimentation and developed FEA model. The results revealed that the percentage difference between FEA model and experimental results was less than 5% in terms of crater depth, crater diameter and lip height.

Microstructural investigations

Figure 12(a) and (b) exhibited the scanning electron micrograph for SLM 3D printed SS316L steel at 400 °C, and 800 °C temperature respectively. The microstructural investigation revealed that the printed material grain boundaries are expanded at elevated temperatures and results in reduction of mechanical properties. Further, Fig. 12(b) (micrograph at 800 °C) shows more coarse grain boundaries than Fig. 12(a) (micrograph at 400 °C).

Conclusions

The following conclusion has been drawn from the current investigation.

(1) The maximum crater depth was achieved at the 800 °C rather than room temperature, 200 °C, 400 °C, and 600 °C for the complete load range 5 to 50 kN.

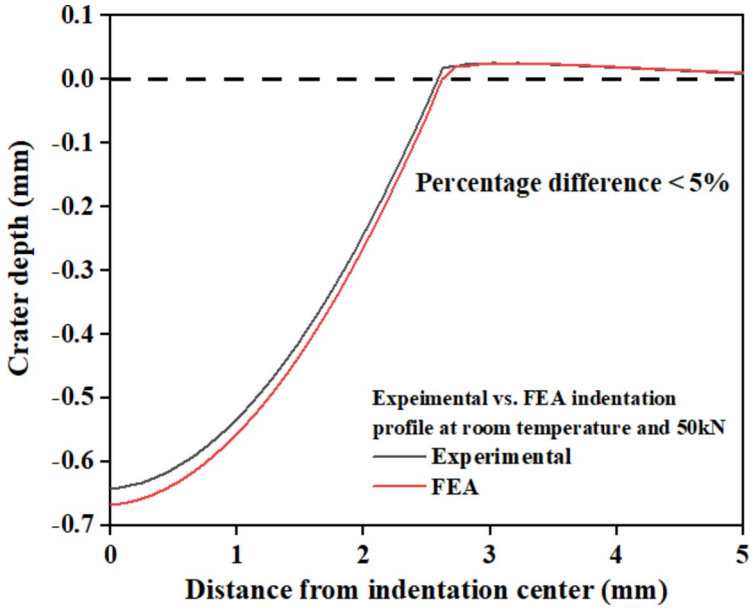

Fig. 11. SLM 3D printed SS316L steel static indentation process FEA results vs. experimental results experimental results.

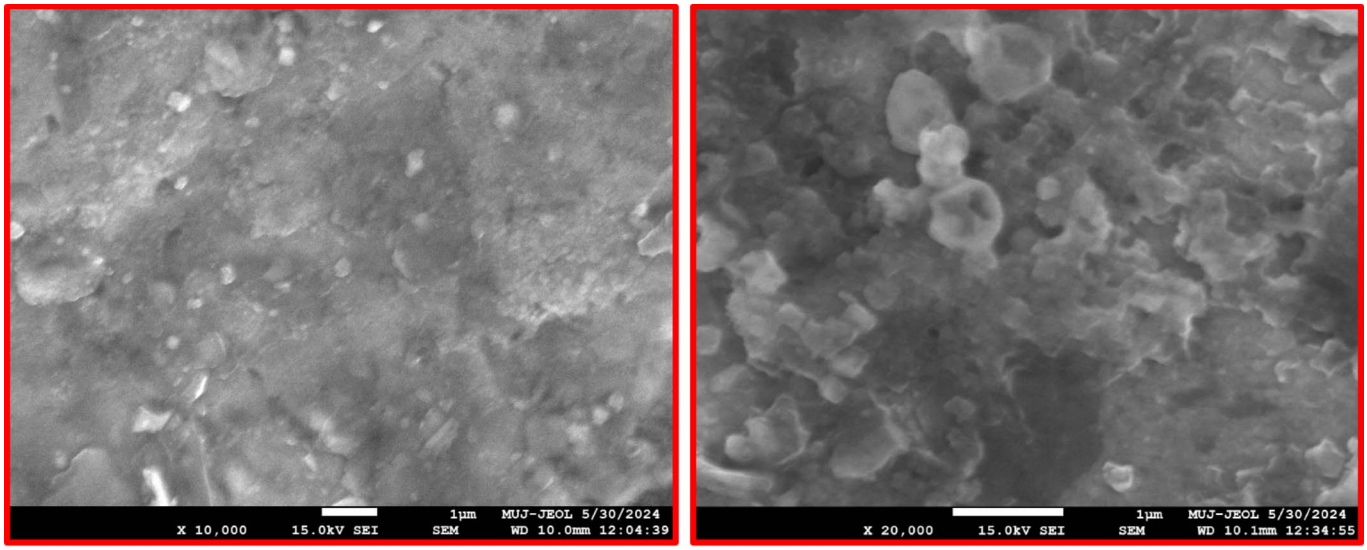

Fig. 12. Scanning electron micrograph for SLM 3D printed SS316L steel at (**a**) 400 °C, (**b**) 800 °C.

(2) The maximum estimated Meyer's hardness values for room temperature, 200 °C, 400 °C, 600 °C and 800 °C were 2342.48, 2115.01, 1884.17, 1528.19 and 1171.80 respectively at 50 kN load.
(3) The Meyer's hardness was reduced 10.20%, 21.68%, 42.07% and 66.62% at 200 °C, 400 °C, 600 °C, and 800 °C respectively, compared with room temperature.
(4) The strain hardening index (p) and indentation strength coefficient (A) values for SLM 3D-printed SS316L steel under confined constrained deformation behavior decrease with the increase in temperature.
(5) The maximum lip height was estimated at 800 °C temperature, 50 kN load and 14.60% average strain. The lip height was increased by 24.34%, 51.40%, 98.29% and 129.22% at 200 °C, 400 °C, 600 °C, and 800 °C respectively, compared with room temperature lip height.
(6) The yield strength of the investigated material was decreased by 8.60%, 27.08%, 55.44% and 75.45% at the 200 °C, 400 °C, 600 °C and 800 °C respectively. Further, the compressive strength was decreased by 9.94%, 30.01%, 61.72% and 88.41% at the 200 °C, 400 °C, 600 °C and 800 °C respectively.

(7) The constraint factor was increased with average strain upto the transition strain after that the CF was constant (independent) for the rest of the average strain. The transition strain was 8.08, 8.26, 8.34, 8.41 and 9.07% average strain for room temperature, 200 °C, 400 °C, 600 °C and 800 °C respectively.
(8) The transition non-dimensional strain values for room temperature, 200 °C, 400 °C, 600 °C and 800 °C were 73.49, 90.81, 98.39, 155.92 and 222.16 respectively.
(9) The results revealed that the percentage difference between developed FEA model and experimental results was less than 5% in terms of crater depth, crater diameter and lip height. This shows the good prediction capability of the material.

Data availability

The datasets generated during and/or analysed during the current study are available in this study. All the characterizations, analysis, testing-related works, and modelings have solely been the responsibility of Ambuj Saxena. Additionally, the raw data can be obtained on request from the corresponding author, Ambuj Saxena.

Received: 4 December 2024; Accepted: 13 March 2025
Published online: 07 April 2025

References

1. Saxena, A., Srivastava, A. K., Maurya, N. K. & Gupta, T. K. Influence of printing orientation on power-law hardening and ductile damage parameters for 3D-printed SS316L steel: experimental and FEA approach. *J. Adhes. Sci. Technol.*, **0**, 1–23 (2024).
2. Suryawanshi, J., Prashanth, K. G. & Ramamurty, U. Mechanical behavior of selective laser melted 316L stainless steel. *Mater. Sci. Engineering: A*. **696**, 113–121 (2017).
3. Murr, L. E. A metallographic review of 3D printing/additive manufacturing of metal and alloy products and components. *Metallography Microstruct. Anal.* **7**, 103–132 (2018).
4. Zheng, L., Liu, Y., Sun, S. & Zhang, H. Selective laser melting of Al–8.5 Fe–1.3 V–1.7 Si alloy: investigation on the resultant microstructure and hardness. *Chin. J. Aeronaut.* **28** (2), 564–569 (2015).
5. Vilaro, T., Colin, C., Bartout, J. D., Nazé, L. & Sennour, M. Microstructural and mechanical approaches of the selective laser melting process applied to a nickel-base superalloy. Materials Science and Engineering: A, 534, pp.446–451. (2012).
6. Ergene, B. & Yalçın, B. Experimental investigation on the mechanical properties of Ti6Al4V cellular structures produced with selective laser melting: Effects of rib thickness, unit cell type and orientation. Proceedings of the Institution of Mechanical Engineers, Part E: Journal of Process Mechanical Engineering, p.09544089241296708. (2024).
7. Ergene, B. *Simulation of the Production of Inconel 718 and Ti6Al4V Biomedical Parts with Different Relative Densities by Selective Laser Melting (SLM) Method* (Journal of the Faculty of Engineering and Architecture of Gazi University, 2022).
8. Sefene, E. M. State-of-the-art of selective laser melting process: A comprehensive review. *J. Manuf. Syst.* **63**, 250–274 (2022).
9. Saxena, A. & Kumaraswamy, A. Numerical analysis of effect of temperature on ball indentation behaviour of Armox500T and IN718. *Trans. Indian Inst. Met.* **71**, 3111–3116 (2018).
10. Saxena, A. & Dwivedi, S. P. Representative volume element (RVE) based FEA investigation on the plastic flow behaviour of friction-stir processed AA7075/Si3N4 composite under constrained deformation conditions. Proceedings of the Institution of Mechanical Engineers, Part E: Journal of Process Mechanical Engineering, p.09544089231193603. (2023).
11. Saxena, A., Kumaraswamy, A., Sethi, S., Madhusudhan Reddy, G. & Madhu, V. Microstructural characterization and high strain rate plastic flow behavior of SMAW Armox500T steel joints from spherical indentation experiments. *J. Mater. Eng. Perform.* **27**, 4261–4269 (2018).
12. Tabor, D. *The Hardness of Metals* (Oxford University Press, 2000).
13. Tabor, D. A simple theory of static and dynamic hardness. In: Proceedings of the Royal Society of London A: Mathematical, Physical and Engineering Sciences, London 4 Feb 1948 (Vol. 192, No. 1029, pp. 247–274). The Royal Society.
14. Subhash, G., Koeppel, B. J. & Chandra, A. Dynamic indentation hardness and rate sensitivity in metals. *J. Eng. Mater. Technol.* **121** (3), 257–263 (1999).
15. Mok, C. H. & Duffy, J. The dynamic stress-strain relation of metals as determined from impact tests with a hard ball. *Int. J. Mech. Sci.* **7** (5), 355–371 (1965).
16. Patnaik, M. N. M., Narasimhan, R. & Ramamurty, U. Spherical indentation response of metallic glasses. *Acta Mater.* **52** (11), 3335–3345 (2004).
17. Saxena, A., Rai, A. & Kumaraswamy, A. A numerical approach to investigate the effect of temperature on constraint factor of Ti alloy under static indentation conditions. *Trans. Indian Inst. Met.* **70**, 1549–1553 (2017).
18. Tirupataiah, Y. & Sundararajan, G. The strain-rate sensitivity of flow stress and strain-hardening rate in metallic materials. *Mater. Sci. Eng. A*. **189** (1–2), 117–127 (1994).
19. Tirupataiah, Y. & Sundararajan, G. A comprehensive analysis of the static indentation process. *Mater. Sci. Eng. A*. **91**, 169–180 (1987).
20. Tirupataiah, Y. & Sundararajan, G. On the constraint factor associated with the indentation of work-hardening materials with a spherical ball. *Metall. Trans. A*. **22** (10), 2375–2384 (1991).
21. Kumaraswamy, A. & Rao, V. V. Effect of temperature on constraint factor of IN718 under static indentation conditions. *Mater. Sci. Eng. A*. **527** (23), 6230–6234 (2010).
22. Kumaraswamy, A. & Venkataraman, B. Effect of temperature on constraint factor of Ti–6Al–4V under static indentation conditions. *Scr. Mater.* **54** (3), 493–498 (2006).
23. Rom, N. & Priel, E. A Data-Driven Methodology for Obtaining the Stress–Strain Curves of Metallic Materials Using Discrete Indentation Tests. Metals, 15(1), p.40. (2025).
24. Saxena, A. et al. Influence of AlCoCrFeNiCuSn HEA reinforcement particles on the plastic flow behaviour of the friction stir processed composite material under constrained confined deformation conditions. Materials Today Communications, 42, p.111084. (2025).
25. Saxena, A. et al. Experimental and numerical investigation of quasi-static (10 – 3 s – 1) fracture behavior of armor steel. *Arab. J. Sci. Eng.* **45** (7), 5623–5629 (2020).
26. Johnson, K. L. The correlation of indentation experiments. *J. Mech. Phys. Solids*. **18** (2), 115–126 (1970).
27. Richmond, O. & Morrison, H. L. ML Devenpeck sphere indentation with application to the Brinell hardness test. *Int. J. Mech. Sci.* **16**, 75–82 (1974).

Acknowledgements

The authors extend their appreciation to the Deanship of Scientific Research at King Khalid University for funding this work through large group Research Project under grant number RGP2/28/44.

Author contributions

Conceptualization, Ambuj Saxena, Neeraj Mishra, Shashi Prakash Dwivedi, N. Beemkumar, Ankit Kedia; methodology, Ambuj Saxena, Neeraj Mishra, Shashi Prakash Dwivedi, N. Beemkumar, Ankit Kedia; formal analysis, Ambuj Saxena, Neeraj Mishra, Shashi Prakash Dwivedi, Shubham Sharma, N. Beemkumar, Ankit Kedia; investigation, Ambuj Saxena, Neeraj Mishra, Shashi Prakash Dwivedi, N. Beemkumar, Ankit Kedia; writing—original draft preparation, Ambuj Saxena, Neeraj Mishra, Shashi Prakash Dwivedi, N. Beemkumar, Ankit Kedia; writing—review and editing, Shubham Sharma, V Nagabhushana Rao, Parveen Kumar, Ehab El Sayed Massoud, Abhinav Kumar, Jasmina Lozanovic; supervision, V Nagabhushana Rao, Parveen Kumar, Ehab El Sayed Massoud, Abhinav Kumar, Jasmina Lozanovic; project administration, V Nagabhushana Rao, Parveen Kumar, Ehab El Sayed Massoud, Abhinav Kumar, Jasmina Lozanovic; funding acquisition, V Nagabhushana Rao, Parveen Kumar, Ehab El Sayed Massoud, Abhinav Kumar, Jasmina Lozanovic. All authors have read and agreed to the published version of the manuscript.

Funding

The authors extend their appreciation to the Deanship of Scientific Research at King Khalid University for funding this work through large group Research Project under grant number RGP2/28/44. In addition, the authors are thankful to the Council of Science and Technology, Uttar-Pradesh (CST, U.P.) (Council of Science and Technology, U.P., Grant/Award Number: CST/D-1313.) for providing financial support to this research.

Declarations

Competing interests

The authors declare no competing interests.

Ethical approval

Not applicable.

Consent to participate

Not applicable.

Consent to publish

All authors have read and approved this manuscript.

Additional information

Correspondence and requests for materials should be addressed to S.S. or J.L.

Reprints and permissions information is available at www.nature.com/reprints.

Publisher's note Springer Nature remains neutral with regard to jurisdictional claims in published maps and institutional affiliations.